2012

Evaluation of Multibody Parafoil Dynamics Using Distributed Miniature Wireless Sensors

Chrystine M. Gorman
University of Alabama - Huntsville

Nathan Slegers
George Fox University, nslegers@georgefox.edu

Evaluation of Multibody Parafoil Dynamics Using Distributed Miniature Wireless Sensors

Chrystine M. Gorman* and Nathan J. Slegers†
University of Alabama in Huntsville, Huntsville, Alabama 35899

Guided parafoils are composed of two primary bodies, a payload and parafoil. The payload encompasses the majority of the overall system mass; however, the parafoil generates the majority of aerodynamic loads and is the sole source of control. Despite the canopy being the source of control, the sensor systems used for guidance are located away from the parafoil. Many multibody models exist in literature and use different degrees of freedom to represent parafoil-payload relative motion. However, in many cases, simulations are used to investigate how the relative motion between bodies affects the overall dynamics without experimental validation determining the accuracy of the motion predicted. The lack of validation for parafoil-payload relative motion has primarily been due to challenges in accurately measuring parafoil canopy motion, which include its flexibility, light weight, need to be packed in a small volume before deployment, and connection through suspension lines to the payload. In this paper, multiple miniature wireless sensors are embedded in the parafoil canopy and payload during flight and are used to measure the parafoil-payload relative motion. Experimental measurements are then compared with a 9 degree-of-freedom model, and relative payload-parafoil motion is analyzed.

Nomenclature

C_{D0}, $C_{D\alpha^2}$ = canopy zero and quadratic angle-of-attack drag coefficients
C_{DS} = payload drag coefficients
C_{L0}, $C_{L\alpha}$ = canopy zero and linear angle-of-attack lift coefficients
C_{lp}, C_{mq}, C_{nr} = canopy roll, pitch, and yaw damping coefficients
$C_{l\delta_a}$, $C_{n\delta_a}$ = canopy lateral control coefficients
C_{m0}, $C_{m\alpha}$ = canopy zero and linear angle-of-attack pitching coefficients
$C_{Y\beta}$ = canopy side force coefficient
$\mathbf{F_A}$, $\mathbf{M_A}$ = parafoil aerodynamic force and moment
$\mathbf{F_C}$, $\mathbf{M_C}$ = internal constraint force and moment
F_{cx}, F_{cy}, F_{cz} = internal constraint force vector components
$\mathbf{F_S}$ = payload drag force
$\mathbf{F_{W_B}}$, $\mathbf{F_{W_S}}$ = parafoil and payload weight
$\mathbf{I_{AM}}$, $\mathbf{I_{AI}}$ = apparent mass and inertia matrices
$\mathbf{I_B}$, $\mathbf{I_S}$ = parafoil and payload inertia matrices
$\mathbf{I}_{N\times N}$ = $N \times N$ identity matrix
$\mathbf{i_B}$, $\mathbf{j_B}$, $\mathbf{k_B}$ = body frame unit vectors
$\mathbf{i_I}$, $\mathbf{j_I}$, $\mathbf{k_I}$ = inertial frame unit vectors
$\mathbf{i_P}$, $\mathbf{j_P}$, $\mathbf{k_P}$ = canopy frame unit vectors
$\mathbf{i_S}$, $\mathbf{j_S}$, $\mathbf{k_S}$ = payload frame unit vectors
K_ψ, K_r = suspension line twisting and damping coefficients
M_{cz} = twist constraint moment in the body frame
m_B = mass of parafoil including canopy and suspension line
m_I = included mass
m_S = mass of the payload
P_B, Q_B, R_B = parafoil roll, pitch, and yaw rate amplitude spectrum
P_S, Q_S, R_S = payload roll, pitch, and yaw rate amplitude spectrum
p_B, q_B, r_B = parafoil angular velocity components in the body frame
p_S, q_S, r_S = payload angular velocity components in the payload frame
R_R, R_L = right and left side canopy yaw rate amplitude spectrum
$\mathbf{r}_{XY}$ = position vector from a point X to a point Y
$\mathbf{S^B_{\omega_B}}$, $\mathbf{S^P_{\omega_B}}$ = cross-product matrices of the parafoil angular velocity in the body and canopy frames.
$\mathbf{S^S_{\omega_S}}$ = cross-product matrix of the payload angular velocity expressed in the payload frame
$\mathbf{S^Z_{r_{XY}}}$ = cross-product matrix of a position vector from a point X to Y expressed in the Z frame
$\mathbf{T_{BP}}$ = transformation from the body to the canopy frame
$\mathbf{T_{BS}}$ = transformation from the body to payload frame
$\mathbf{T_{IB}}$ = transformation from the inertial to body frame
u_c, v_c, w_c = connection point velocity components expressed in the body frame
$\mathbf{V_{A/I}}$ = wind velocity vector expressed in the inertial frame
$\mathbf{V_C}$ = velocity of connection point C
$\mathbf{V}$ = canopy aerodynamic velocity expressed in the canopy frame
x_c, y_c, z_c = connection point position components
Γ = canopy incidence angle
ϕ_B, θ_B, ψ_B = Euler roll, pitch, and yaw angles of the parafoil body
ϕ_S, θ_S, ψ_S = angles of the payload relative to the parafoil body
$\boldsymbol{\omega_B}$, $\boldsymbol{\omega_S}$ = parafoil and payload angular velocities in their respective frames
$\boldsymbol{\omega_{S/B}}$ = angular velocity of the payload with respect to the parafoil expressed in the payload frame
$\mathbf{0}_{N\times N}$ = $N \times N$ zero matrix

Subscript

B = parafoil body
I = inertial frame

Presented as Paper 2011-2615 at the 21st AIAA Aerodynamic Decelerator Systems Technology Conference and Seminar, Dublin, Ireland, 23–26 May 2011; received 24 June 2011; revision received 24 October 2011; accepted for publication 25 October 2011.

*Graduate Student, Department of Mechanical and Aerospace Engineering. Student Member AIAA.

†Associate Professor, Department of Mechanical and Aerospace Engineering; slegers@mae.uah.edu. Senior Member AIAA (Corresponding Author).

P = parafoil canopy
S = payload

I. Introduction

IMPROVEMENT in precision airdrop through advanced guidance and improved modeling has been driven by focused efforts in developing these systems. An example of such an effort is the U.S. Department of Defense's Joint Precision Airdrop System (JPADS) programs [1,2]. Parafoil systems have many characteristics that make them challenging to accurately model. For example, the canopy, where the majority of aerodynamic forces originate, has a small mass-to-volume ratio, resulting in apparent mass forces and moments [3], whereas the payload dominates the total system weight. Another challenging aspect is that canopy and suspension lines create a flexible structure, allowing for the possibility of changing shapes and aerodynamics. In addition, the payload and canopy can be connected using many configurations. Models approximating actual connections of the payload can allow for motion, including both translation and rotation, where relative rotation can range from free rotation of the payload with respect to the parafoil to a rigid canopy-payload connection.

In some applications, certain characteristics of the parafoil and payload can be ignored, resulting in a range of models with varying degrees of freedom (DOF). The simplest models neglect some of the translation and rotation DOF, resulting in models with less than 6 DOF, as discussed by Jann [4]. Models including more complete system dynamics systems using 6 DOF, where the payload and parafoil are approximated as one rigid body, are commonly used [5–8]. In contrast to the 6-DOF model, separation of the parafoil and payload rotation by a confluence point allows the payload to freely rotate with respect to the canopy, resulting in 9 DOF. Both Slegers and Costello [9] and, then, Mooij et al. [10] developed 9-DOF models for parafoil systems using different approaches. Actual parafoil and payloads are not attached by a theoretical confluence point, but rather, by risers that constrain the parafoil and payload pitch and roll. Kinematic coupling of one or more of the body rotations results in models between 6 and 9 DOF. As examples, models considering 8 DOF have been developed by Müller et al. [11], Redelinghuys [12], and Slegers [13], where both analytic and Newtonian dynamics have been used. Strickert and Witte [14] and Strickert [15] took a different approach by including translation of the parafoil with respect to payload resulting from the harness, lines, and canopy flexibility. Analysis was based on a multibody simulation package integrated with a simulated aerodynamic model. To establish an overall model of relative motion, both the aerodynamic and multibody models were computed simultaneously.

In practical applications, the simplest model that captures all the important dynamics is preferred. The existence of multibody parafoil models with varying DOF forces the user to determine which of the relative parafoil-payload DOF should be included; namely yaw, pitch, and roll of the payload with respect to the parafoil canopy or possibly none. The literature includes many multibody models; however, in almost every case, simulation alone has been the tool used to analyze contributions of the relative parafoil-payload motion. Another challenge in determining an appropriate model DOF is, that for a given system with a specific parafoil-payload connection, the designer can frequently justify 6-, 7-, 8-, and 9-DOF models to themselves and others.

To effectively understand parafoil-payload motion, the comparison of proposed models with experimental data is required. and analysis beyond simulation alone must be pursued. Measurement of parafoil-payload relative motion has always been challenging due to the flexible nature of the canopy and requires a sensing system that does not interfere with canopy packing, does not significantly increase the canopy mass, and requires no physical connection between the canopy and payload. In 1999, Strickert and Jann [16] successfully used video-image processing techniques to measure parafoil-payload relative motion. Post-flight analysis demonstrated the difficulty in estimating the differences in the orientation of the payload and canopy. Later, Strickert and Witte [14] and Strickert [15] used the same video-measurement system, and a multibody simulation was used primarily to investigate relative longitudinal displacement, lateral displacement, and yawing. In this paper, the authors take a different approach by embedding multiple miniature low-power wireless inertial sensors into the canopy. After release, the canopy sensors transmit inertial data to a main payload flight computer in flight. Information provided from each sensor includes orientation, angular velocity, and accelerations. Finally, a 9-DOF model is compared with experimental data to show how each payload rotation mode compares with the test system.

II. Experimental Platform

The deployed experimental parafoil system is shown in Fig. 1 and is similar to the system used in Slegers et al. [17] and Yakimenko et al. [18]. The payload is rectangular with a drag area of 0.042 m^2 and a mass of 1.92 kg. The parafoil canopy and suspension lines have a combined mass of 0.21 kg and an included air mass of 0.091 kg. The canopy has a span of 1.36 m, mean chord of 0.69 m, incidence angle Γ of -12 deg, and maximum control deflection of 23 cm. Connection of the parafoil canopy and payload is achieved through a four-point riser connection at the top of the payload, as shown in detail in Fig. 2.

The geometry of the four connection points can significantly alter the relative motion between the parafoil canopy and payload. Figure 3 shows possible connections that lead to simplified 6- to 9-DOF models, where effects, such as canopy flexibility and relative payload translation, as discussed by Strickert [15], are neglected. If all four connections coincide at the center, then a theoretical confluence point of a 9-DOF model is closely represented. In contrast, if the distances of the connections are sufficiently large, then no significant payload relative yaw, pitch, or roll is allowed unless the risers twist, stretch, or become slack, and the 6-DOF model connection is closely approximated. When connection distances are moderate, the payload may be able to twist about its vertical axis, without risers stretching or becoming slack, and an ideal 7-DOF model with only relative parafoil-payload twist is closely represented. Connections coinciding as two pairs, with no separation in the fore-aft or left-right direction, mimic free pitching or rolling, respectively. Such

Fig. 1 Parafoil-payload experimental system.

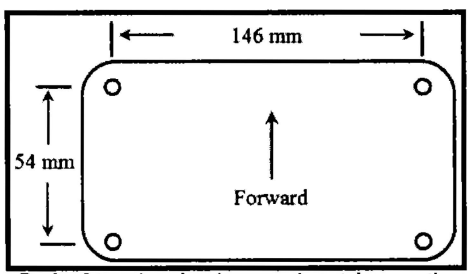

Fig. 2 Payload top view showing experimental connection points.

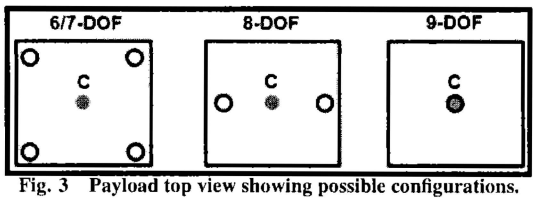

Fig. 3 Payload top view showing possible configurations.

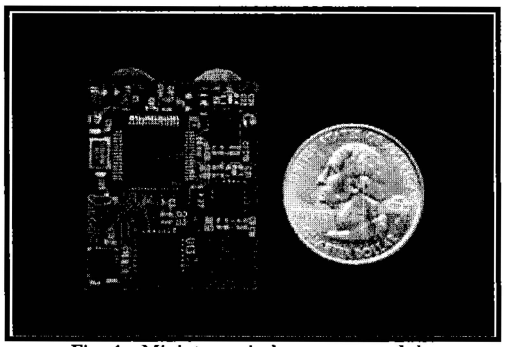
Fig. 4 Miniature wireless sensor module.

configurations are represented by 8-DOF models, which include relative twist and either relative roll or pitch.

Inspection of the experimental riser connection in Fig. 2 demonstrates that none of the theoretical 6- to 9-DOF configurations is represented exactly. Although the experimental system connection is located as far apart as the payload geometry will allow, they are still close enough that twisting, pitching, and rolling may be expected. The experimental configuration was chosen because it achieved a high level of restriction to parafoil-payload relative motion for the system. In general, modelers could reasonably justify any of the models ranging from 6 to 9 DOF.

The entire experimental sensor system is made up of two components, a set of miniature wireless sensor modules (MWSM), as shown in Fig. 4, and the main flight computer. The MWSM is 11 cm^2, which is roughly the size of a U.S. quarter, and weighs about 10 grams, including the battery, which is less than the weight of two U.S. quarters. The MWSM includes a 32-bit microprocessor, temperature sensor, three gyroscopes, three accelerometers, three magnetometers, and a low-power wireless transceiver with 20 m range.

The MWSM has two modes, online and sleep. In the online mode, the sensor calculates orientation and temperature compensated data at 100 Hz. In sleep mode, the system maintains an ultralow power state waiting for a prompt from the flight computer, which then initiates the online mode. The battery life of the sensor while sleeping is about 12–36 hr, depending on the desired sensor activation response time. The long sleep duration allows the system to be packed in the canopy overnight. When the sensor is fully online, the MWSM can run continuously for about 2 hr. The flight computer has the same inertial sensors and ultralow power wireless transceiver as the MWSM but also includes a Global Positioning System, servo controllers, external memory, and a midrange wireless transceiver.

Two MWSMs were sewn to the canopy inside the cells using small holes around the sensor edge, as visible in Fig. 4. The MWSMs were placed at a quarter-chord of canopy, 27 cm away from the canopy centerline, as shown in Fig. 5. This setup provided the ability to measure potential canopy bending as well as redundancy.

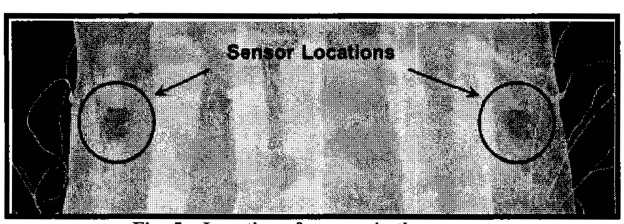

Fig. 5 Location of sensors in the canopy.

III. Experimental Data

The experimental parafoil system was released from an altitude of 400 m, and data were recorded from both canopy sensors and the payload at 12 Hz. During the approximately 80 s before touchdown, a series of left and right turns were made using brake deflections ranging from 40% to 60% of the maximum range. Figures 6 and 7 show the amplitude spectrum of measured angular velocities for both the payload and parafoil canopy, where P_s, Q_s, and R_s are the payload roll rate, pitch rate, and yaw rate amplitude spectrums, respectively, and P_B, Q_B, and R_B are the canopy roll rate, pitch rate, and yaw rate amplitude spectrums. From Fig. 6, it is observed that the payload roll and pitch rate amplitude spectrums have similar components at 2.1 and 2.3 Hz, respectively. Both the payload roll rate and pitch rate frequencies are approximately 50% higher than that of an ideal pendulum. This is consistent with the double pendulum nature of the parafoil and payload system, where a simple linearized double pendulum experiences a frequency mode that is larger than a single pendulum and can vary dramatically as a function of pendulum length and mass ratios [19]. The payload yaw rate has two components, a low-frequency component at 0.05 Hz from the control input and a dynamic twisting mode at 1.05 Hz. The 0.5 Hz frequency component is generated by the change in left and right turns at approximately 20 s intervals during experiments.

Angular velocity amplitude spectrums for the total canopy are found by combining data from both canopy sensors into one signal using their mean and, therefore, representing the average canopy motion. The canopy pitch rate amplitude spectrum in Fig. 7 has a peak at 2.3 Hz, near that of the payload pitch rate but of lesser magnitude and is a result of the two bodies' pitch coupling, as will be shown in Section V. Both the canopy roll and yaw rates have a significant component at 0.05 Hz related to the control input and show the coupling between rolling and yawing of the canopy during turns. In addition, the canopy has a 0.85 Hz roll rate componen,t where some minor coupling between the canopy and payload can be observed. The 1.05 Hz payload twist mode does not appear in the parafoil yaw rate.

If the commonly used 6-DOF model were adequate to model the parafoil-payload system, then the two sets of amplitude spectrums in Figs. 6 and 7 should be very similar. However, this is not the case, and significant modes are either missing as in the roll and yaw rates or have different magnitudes as in the pitch rate, demonstrating more than 6 DOF may be necessary.

Canopy sensors located symmetrically on the left and right side of the canopy provide the potential to identify symmetric bending dynamic modes. In contrast to the angular velocity amplitude

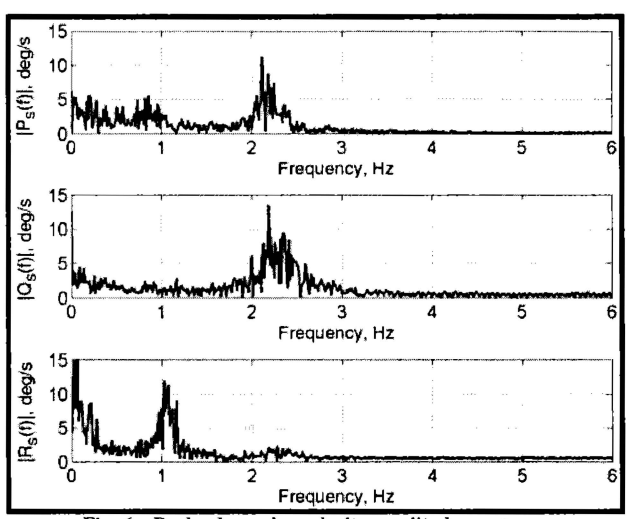

Fig. 6 Payload angular velocity amplitude spectrum.

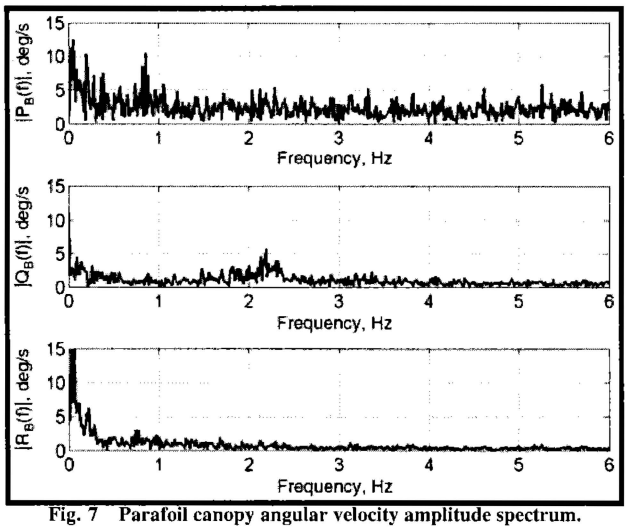

Fig. 7 Parafoil canopy angular velocity amplitude spectrum.

spectrums in Figs. 6 and 7, where the total canopy angular velocity is the average of left and right sensors, the amplitude spectrum of individual sensors can be investigated. If the canopy rotates as a rigid body, then the left- and right-side sensors would have the same angular velocity with the average having the same amplitude spectrum at each sensor. However, when the canopy bends, left and right sensors have opposing angular velocities, which negate each other when taking the average. The bending mode frequency is, then, absent from the average amplitude spectrum but present in the individual sensors. This later case is demonstrated in Fig. 8 for the canopy bending about its vertical axis, where R_R, R_L, and R_B are the right-side canopy yaw rate, left-side canopy raw rate, and average canopy yaw rate amplitude spectrums, respectively.

Both left and right sensors exhibit a 0.05 Hz component from the yaw rate commanded by control inputs and a smaller 2.2 Hz yaw rate component. When the time domain signals are averaged, the 2.2 Hz components disappear, and only the 0.05 Hz yaw rate mode remains, demonstrating that the canopy has a 0.05 Hz rigid-body-turning mode and a 2.2 Hz symmetric-bending mode. Figure 9 illustrates a top view of one possible type of canopy motion for this bending phenomenon, where the canopy symmetrically bends fore and aft. Other types of deformation modes, such as trapezoidal deformation where the leading edge narrows more than the trailing edge and vice versa, could also result in differences in yaw rate.

The phenomenon is commonly referred to as accordioning or breathing. As the canopy breathes in and out, the angle of attack in the

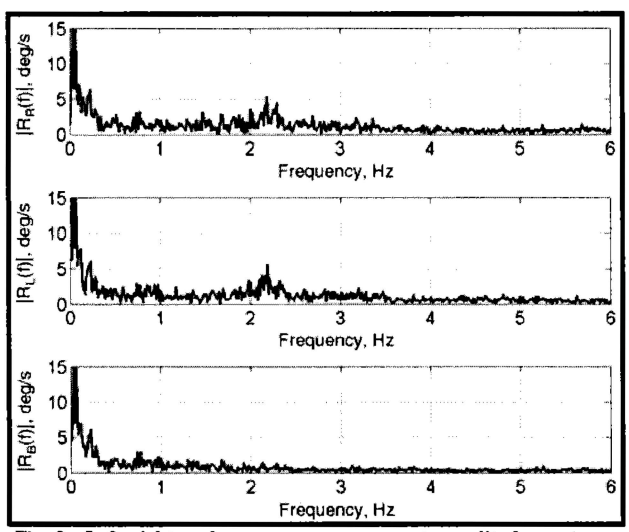

Fig. 8 Left, right, and average canopy yaw rate amplitude spectrum.

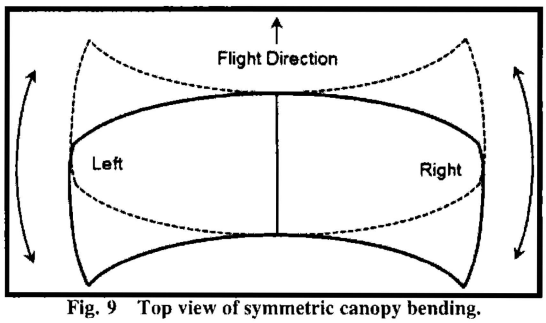

Fig. 9 Top view of symmetric canopy bending.

tips may change, altering the canopy performance. The cause is insufficient rigidity in the inflated structure. The canopy breathing frequency is the same as the payload roll and pitch rate frequencies, which demonstrate that the payload relative motion and this phenomenon may be coupled. Analysis of the canopy roll and pitch rates failed to identify any similar symmetric bending modes. This suggests that the canopy is effectively rigid with the exception of a higher frequency symmetric bending or breathing mode about its vertical axis, which is small in magnitude compared with the rigid mode.

Comparisons between the payload and parafoil measurements are shown in Figs. 10–13. Angular rate data come directly from the gyroscopes; roll and pitch angles are derived from a nonlinear filter using both gyroscopes and accelerometers; and the yaw angle comes from a nonlinear filter using the gyroscopes and magnetometers. All computations are done in real time on the MWSM. The yaw rate is separated into two figures because of the large twisting motion just after the canopy inflates. During canopy inflation, it is common for the payload to twist multiple times before reaching equilibrium. Figure 10, starting immediately after canopy inflation, shows the payload yaw rate oscillating with an initial amplitude of 400 deg/s and decaying over six to seven cycles. The parafoil oscillates in response to the payload and line twisting, lagging behind 90 deg in phase with a significantly smaller initial amplitude of approximately 50 deg/s.

Payload and canopy yaw, yaw rate, and control deflection after the initial payload untwisting are shown in Fig. 11. The 1.05 Hz payload twisting mode is clearly evident in the payload yaw rate, r_x, and persists with amplitudes ranging from 20 to 30 deg/s. The payload-twisting-mode amplitude is on the same order as the slower yaw rate during turning. The parafoil also exhibits a small 1.05 Hz oscillation in response to the payload, but its amplitude is 5 to 10 deg/s and is small compared with the larger amplitude yaw rate during turning.

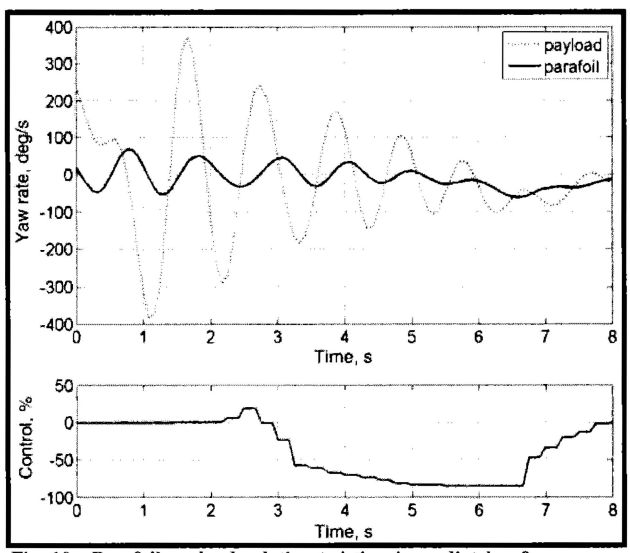

Fig. 10 Parafoil-payload relative twisting immediately after canopy inflation.

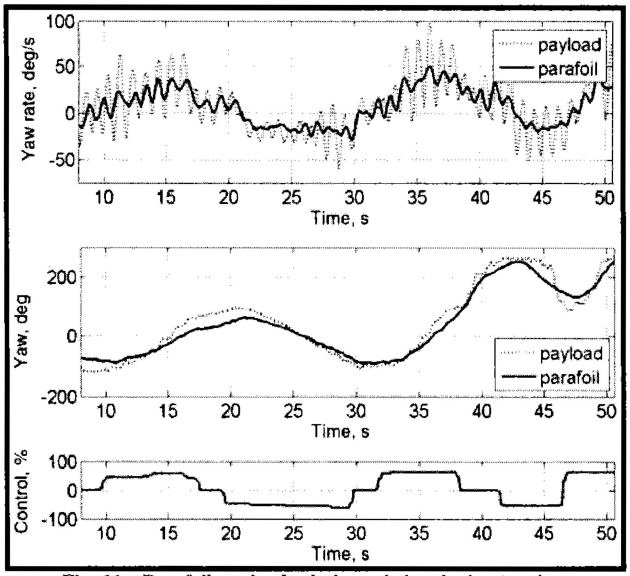

Fig. 11 Parafoil-payload relative twisting during turning.

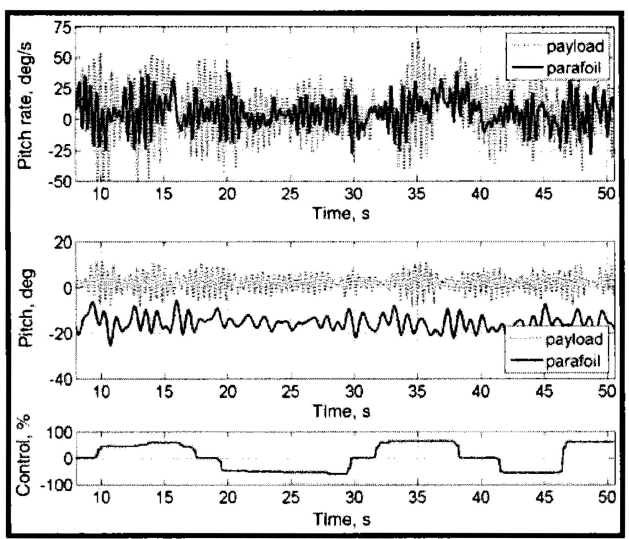

Fig. 12 Pitch and pitch rate of the parafoil canopy and payload.

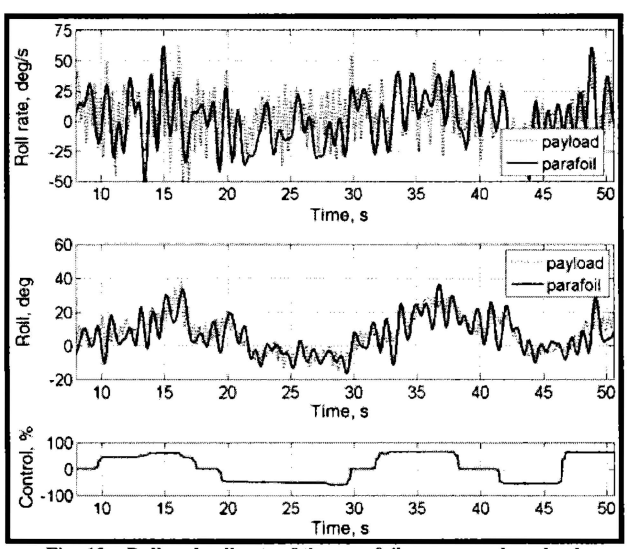

Fig. 13 Roll and roll rate of the parafoil canopy and payload.

Pitch rates of both the payload and canopy primarily exhibit a 2.3 Hz oscillation that is excited during most of the flight. Throughout turning, the pitch angle remains close to 0 and -16 deg for the payload and parafoil with only small variations, as seen in Fig. 12. Rolling dynamics are shown in Fig. 13, where differences in the payload and canopy roll-rate frequencies can be seen. In contrast to the pitch angle, the payload roll varies by approximately 20 deg as the system turns with positive roll during a right turn (positive control) and negative roll during a left turn (negative control). The parafoil roll exhibits a similar trend. Common to all measured payload and parafoil angular velocities are persistent oscillations throughout the flight. In Fig. 10, the initially large payload yaw rate decays from 400 deg/s to 30 deg/s in six to seven cycles. Similarly both pitch and roll rates experience persistent oscillations.

IV. Dynamic Model

The preceding experimental results demonstrate that, although the risers connecting the parafoil canopy and payload were located to resist relative payload motion as much as possible, relative payload motion still persisted and could be quantified. Comparisons between the experimental results and a multibody model were achieved using a 9-DOF model. Using a 9-DOF two-body system, as shown in Figs. 14 and 15, three coordinate frames were defined to develop the model. Such coordinate frames include a body frame (B) fixed at the body mass center that includes the canopy and suspension lines, a parafoil canopy frame (P) fixed to the canopy aerodynamic center, and a payload frame (S). Other points defined include the canopy reference point R and the apparent mass center M. The reference point R is any fixed reference point on the canopy. The authors use the point directly above the rear suspension lines as a reference. System DOFs include three inertial position components of the connection point C (x_C, y_C, z_C), three Euler orientation angles of the body (yaw ψ_B, pitch θ_B, and roll ϕ_B), and three Euler orientation angles of the payload (yaw ψ_s, pitch θ_s, and roll ϕ_s).

The body frame orientation is obtained by a sequence of three body-fixed rotations using Euler yaw ψ_B, pitch θ_B, and roll ϕ_B. Orientation of the parafoil canopy frame with respect to the body frame is defined as the incidence angle Γ about R and is a constant for the system. Transformations from the inertial to body frame and from body frame to canopy frame can be written as

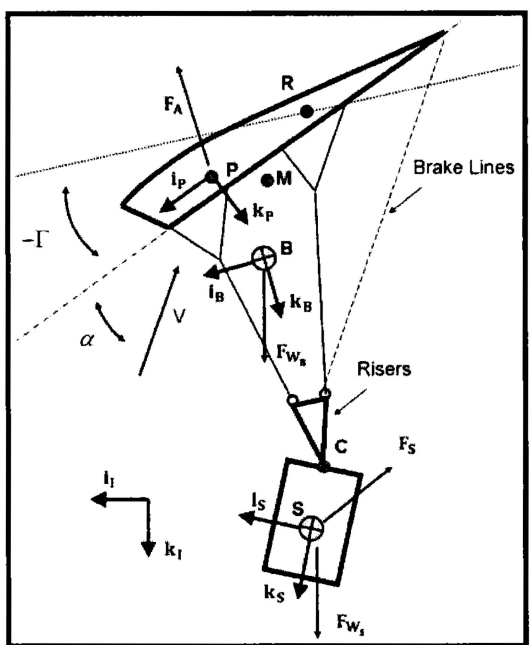

Fig. 14 Parafoil-payload side view.

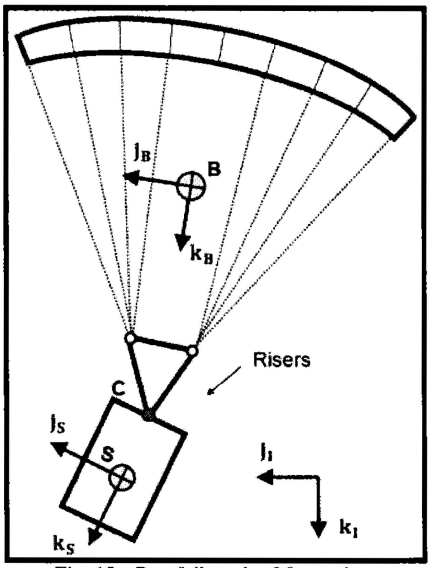

Fig. 15 Parafoil-payload front view.

$$\mathbf{T}_{\mathbf{IB}} = \begin{bmatrix} c_{\theta_B} c_{\psi_B} & c_{\theta_B} s_{\psi_B} & -s_{\theta_B} \\ s_{\phi_B} s_{\theta_B} c_{\psi_B} - c_{\phi_B} s_{\psi_B} & s_{\phi_B} s_{\theta_B} s_{\psi_B} + c_{\phi_B} c_{\psi_B} & s_{\phi_B} c_{\theta_B} \\ c_{\phi_B} s_{\theta_B} c_{\psi_B} + s_{\phi_B} s_{\psi_B} & c_{\phi_B} s_{\theta_B} s_{\psi_B} - s_{\phi_B} c_{\psi_B} & c_{\phi_B} c_{\theta_B} \end{bmatrix} \tag{1}$$

$$\mathbf{T}_{\mathbf{BP}} = \begin{bmatrix} c_r & 0 & -s_r \\ 0 & 1 & 0 \\ s_r & 0 & c_r \end{bmatrix} \tag{2}$$

using common shorthand notation for trigonometric functions of $\sin(\sigma) \equiv s_\sigma, \cos(\sigma) \equiv c_\sigma$, and $\tan(\sigma) \equiv t_\sigma$. The payload frame ($S$) is fixed at the mass center of the payload, and its orientation is obtained by starting from the body frame then rotating through a similar sequence of three body-fixed rotations, ψ_s, θ_s, and ϕ_s. Transformation from the body to payload frame can be written as

$$\mathbf{T}_{\mathbf{BS}} = \begin{bmatrix} c_{\theta_s} c_{\psi_s} & c_{\theta_s} s_{\psi_s} & -s_{\theta_s} \\ s_{\phi_s} s_{\theta_s} c_{\psi_s} - c_{\phi_s} s_{\psi_s} & s_{\phi_s} s_{\theta_s} s_{\psi_s} + c_{\phi_s} c_{\psi_s} & s_{\phi_s} c_{\theta_s} \\ c_{\phi_s} s_{\theta_s} c_{\psi_s} + s_{\phi_s} s_{\psi_s} & c_{\phi_s} s_{\theta_s} s_{\psi_s} - s_{\phi_s} c_{\psi_s} & c_{\phi_s} c_{\theta_s} \end{bmatrix} \tag{3}$$

A. Kinematics and Dynamics

The velocity of connection point C and the angular velocity of the parafoil body with respect to the inertial frame (I) are both defined in the body frame (B) as

$$\mathbf{V}_\mathbf{c} = u_c \mathbf{i}_\mathbf{B} + v_c \mathbf{j}_\mathbf{B} + w_c \mathbf{k}_\mathbf{B} = \begin{Bmatrix} u_c \\ v_c \\ w_c \end{Bmatrix} \tag{4}$$

$$\boldsymbol{\omega}_\mathbf{B} = p_B \mathbf{i}_\mathbf{B} + q_B \mathbf{j}_\mathbf{B} + r_B \mathbf{k}_\mathbf{B} = \begin{Bmatrix} p_B \\ q_B \\ r_B \end{Bmatrix} \tag{5}$$

resulting in translation and rotational kinematic equations for the parafoil body being expressed as

$$\begin{Bmatrix} \dot{x}_c \\ \dot{y}_c \\ \dot{z}_c \end{Bmatrix} = \mathbf{T}_{\mathbf{IB}}^T \begin{Bmatrix} u_c \\ v_c \\ w_c \end{Bmatrix} \tag{6}$$

$$\begin{Bmatrix} \dot{\phi}_B \\ \dot{\theta}_B \\ \dot{\psi}_B \end{Bmatrix} = \begin{bmatrix} 1 & s_{\theta_B} t_{\theta_B} & c_{\theta_B} t_{\theta_B} \\ 0 & c_{\phi_B} & -s_{\phi_B} \\ 0 & s_{\phi_B}/c_{\theta_B} & c_{\phi_B}/c_{\theta_B} \end{bmatrix} \begin{Bmatrix} p_B \\ q_B \\ r_B \end{Bmatrix} \tag{7}$$

The angular velocity of the payload with respect to the inertial frame (I) can be defined in the payload frame (S) and written as

$$\boldsymbol{\omega}_\mathbf{S} = p_S \mathbf{i}_\mathbf{S} + q_S \mathbf{j}_\mathbf{S} + r_S \mathbf{k}_\mathbf{S} = \begin{Bmatrix} p_S \\ q_S \\ r_S \end{Bmatrix} \tag{8}$$

and can also be written using the payload-canopy relative angular velocity as

$$\boldsymbol{\omega}_\mathbf{S} = \mathbf{T}_{\mathbf{BS}} \boldsymbol{\omega}_\mathbf{B} + \boldsymbol{\omega}_{\mathbf{S/B}} \tag{9}$$

Expressing the Euler angle kinematics of $\boldsymbol{\omega}_{\mathbf{S/B}}$ in a similar form as Eq. (7) and combining it with Eq. (9) results in the payload kinematic equations

$$\begin{Bmatrix} \dot{\phi}_S \\ \dot{\theta}_S \\ \dot{\psi}_S \end{Bmatrix} = \begin{bmatrix} 1 & s_{\theta_S} t_{\theta_S} & c_{\theta_S} t_{\theta_S} \\ 0 & c_{\phi_S} & -s_{\phi_S} \\ 0 & s_{\phi_S}/c_{\theta_S} & c_{\phi_S}/c_{\theta_S} \end{bmatrix} \left(\begin{Bmatrix} p_S \\ q_S \\ r_S \end{Bmatrix} - \mathbf{T}_{\mathbf{BS}} \begin{Bmatrix} p_B \\ q_B \\ r_B \end{Bmatrix} \right) \tag{10}$$

The payload kinematic equations here differ from those in some previous 9-DOF models, notably Slegers and Costello [9], because the payload orientation is defined with respect to the body (B) instead of than the inertial frame (I). The difference facilitates analysis of relative canopy-payload motion because ψ_s, θ_s, and ϕ_s are now the difference between the parafoil body (B) and payload (S), rather than between the inertial frame (I) and payload (S). It is important to note that, when the parafoil body and payload are aligned ψ_s, θ_s, and ϕ_s will be zero regardless of the parafoil body orientation. Another advantage that will be seen in the next section is that the proposed definition greatly simplifies the definition of a payload-twisting restraint.

The equations of motion for the 9-DOF model are formed by separating the parafoil body and payload at the confluence point, exposing the constraint forces and moments. Four vector equations can be formed, two by equating the time derivative of linear momentum with the total forces on each body, and two by equating the time derivative of angular momentum with the total moment on each body. The required accelerations of the body frame (B) and payload frame (S) for all models are

$$\mathbf{a}_{\mathbf{B/I}} = \dot{\mathbf{V}}_\mathbf{c} + \mathbf{S}^\mathbf{B}_{\boldsymbol{\omega}_\mathbf{B}} \mathbf{V}_\mathbf{c} - \mathbf{S}^\mathbf{B}_{\mathbf{r_{CB}}} \boldsymbol{\alpha}_\mathbf{B} + \mathbf{S}^\mathbf{B}_{\boldsymbol{\omega}_\mathbf{B}} \mathbf{S}^\mathbf{B}_{\boldsymbol{\omega}_\mathbf{B}} \mathbf{r}_{\mathbf{CB}} \tag{11}$$

$$\mathbf{a}_{\mathbf{S/I}} = \mathbf{T}_{\mathbf{BS}} (\dot{\mathbf{V}}_\mathbf{c} + \mathbf{S}^\mathbf{B}_{\boldsymbol{\omega}_\mathbf{B}} \mathbf{V}_\mathbf{c}) - \mathbf{S}^\mathbf{S}_{\mathbf{r_{CS}}} \boldsymbol{\alpha}_\mathbf{S} + \mathbf{S}^\mathbf{S}_{\boldsymbol{\omega}_\mathbf{S}} \mathbf{S}^\mathbf{S}_{\boldsymbol{\omega}_\mathbf{S}} \mathbf{r}_{\mathbf{CS}} \tag{12}$$

where the convention for the vector cross product of two vectors $\mathbf{r} = [r_x \quad r_y \quad r_z]^T$ and $\mathbf{F} = [F_x \quad F_y \quad F_z]^T$, both expressed in an A reference frame, is written as

$$\mathbf{S}^\mathbf{A}_\mathbf{r} \mathbf{F} = \begin{bmatrix} 0 & -r_z & r_y \\ r_z & 0 & -r_x \\ -r_y & r_x & 0 \end{bmatrix} \tag{13}$$

The derivative of angular momentum for the parafoil body and payload in their respective frames are expressed as

$$\frac{\mathrm{d}}{\mathrm{d}t} \mathbf{H}_{\mathbf{B/I}} = \mathbf{I}_\mathbf{B} \dot{\boldsymbol{\omega}}_\mathbf{B} + \mathbf{S}^\mathbf{B}_{\boldsymbol{\omega}_\mathbf{B}} \mathbf{I}_\mathbf{B} \boldsymbol{\omega}_\mathbf{B} \tag{14}$$

$$\frac{\mathrm{d}}{\mathrm{d}t} \mathbf{H}_{\mathbf{S/I}} = \mathbf{I}_\mathbf{S} \dot{\boldsymbol{\omega}}_\mathbf{S} + \mathbf{S}^\mathbf{S}_{\boldsymbol{\omega}_\mathbf{S}} \mathbf{I}_\mathbf{S} \boldsymbol{\omega}_\mathbf{S} \tag{15}$$

B. Forces and Moments

Forces and moments acting on the system from weight, aerodynamics, and apparent mass are similar to those in Slegers [13] and are not repeated here. However, constraint forces and moment at confluence are different from Slegers [13] due to the lack of a rolling constraint. Internal constraint forces and moments for the 9-DOF model, expressed in the body frame, are defined as

$$\mathbf{F}_C = F_{cx}\mathbf{i}_B + F_{cy}\mathbf{j}_B + F_{cz}\mathbf{k}_B = \begin{Bmatrix} F_{cx} \\ F_{cy} \\ F_{cz} \end{Bmatrix} \tag{16}$$

$$\mathbf{M}_C = M_{cz}\mathbf{k}_S \tag{17}$$

where M_{cz} is the known line-twist moment and is dependent on the parafoil-payload connection and riser geometry, which can vary dramatically from system to system. In this case, the line twist is modeled as a rotational spring and damper, where both the stiffness K_ψ and damping coefficients K_r may be functions of ψ_s:

$$M_{cz} = K_\psi(\psi_s)\psi_s + K_r(\psi_s)r_s \tag{18}$$

C. Equations of Motion

Dynamic equations of motion and constraint forces may be found using Newtonian dynamics and can be written in matrix form similar to Slegers [13], where each row equation is found by either equating the sum of forces to the derivative of linear momentum or equating a moment summation to the derivative of angular momentum for the parafoil and payload. The 9-DOF dynamics are given in Eqs. (19–23), with the first and second row equations found by summing the forces on the payload and parafoil in their respective frames and using Eqs. (11) and (12); the third and fourth are obtained by summing the moments about payload and parafoil mass centers, in their respective frames, and using (14) and (15). The common convection of $\mathbf{I}'_x = \mathbf{T}_{BP}^T\mathbf{I}_x\mathbf{T}_{BP}$ was used for similarity transformations in Eq. (19), (21), and (23).

$$\begin{bmatrix} -m_s\mathbf{S}^S_{r_{CS}} & \mathbf{0}_{3\times3} & m_s\mathbf{T}_{BS} & -\mathbf{T}_{BS} \\ \mathbf{0}_{3\times3} & -(m_B+m_I)\mathbf{S}^B_{r_{CB}} - \mathbf{I}'_{AM}\mathbf{S}^B_{r_{CM}} & (m_B+m_I)\mathbf{I}_{3\times3} + \mathbf{I}'_{AM} & \mathbf{I}_{3\times3} \\ \mathbf{I}_S & \mathbf{0}_{3\times3} & \mathbf{0}_{3\times3} & \mathbf{S}^S_{r_{CS}}\mathbf{T}_{BS} \\ \mathbf{0}_{3\times3} & \mathbf{I}_B + \mathbf{I}'_{AI} - \mathbf{S}^B_{r_{BM}}\mathbf{I}'_{AM}\mathbf{S}^B_{r_{CM}} & \mathbf{S}^B_{r_{BM}}\mathbf{I}'_{AM} & -\mathbf{S}^B_{r_{CB}} \end{bmatrix} \begin{Bmatrix} \dot{p}_s \\ \dot{q}_s \\ \dot{r}_s \\ \cdots \\ \dot{p}_B \\ \dot{q}_B \\ \dot{r}_B \\ \cdots \\ \dot{u}_c \\ \dot{v}_c \\ \dot{w}_c \\ \cdots \\ F_{cx} \\ F_{cy} \\ F_{cz} \end{Bmatrix} = \begin{Bmatrix} \mathbf{B}_1 \\ \cdots \\ \mathbf{B}_2 \\ \cdots \\ \mathbf{B}_3 \\ \cdots \\ \mathbf{B}_4 \end{Bmatrix} \tag{19}$$

$$\mathbf{B}_1 = \mathbf{F}_S + \mathbf{F}_{W_S} - m_s\mathbf{S}^S_{\omega_S}\mathbf{S}^S_{\omega_S}\mathbf{r}_{CS} - m_s\mathbf{T}_{BS}\mathbf{S}^B_{\omega_B}\mathbf{V}_c \tag{20}$$

$$\mathbf{B}_2 = \mathbf{F}_A + \mathbf{F}_{W_B} - (m_B+m_I)\mathbf{S}^B_{\omega_B}\mathbf{V}_c - (m_B+m_I)\mathbf{S}^B_{\omega_B}\mathbf{S}^B_{\omega_B}\mathbf{r}_{CB} - \mathbf{T}^T_{BP}\mathbf{S}^P_{\omega_B}\mathbf{I}_{AM}\bar{\mathbf{V}} - \mathbf{I}'_{AM}\mathbf{S}^B_{\omega_B}\mathbf{T}_{IB}\mathbf{V}_{A/I} \tag{21}$$

$$\mathbf{B}_3 = \mathbf{T}_{BS}\mathbf{M}_c - \mathbf{S}^S_{\omega_S}\mathbf{I}_S\omega_S \tag{22}$$

$$\mathbf{B}_4 = \mathbf{M}_A + \mathbf{S}^B_{r_{BA}}\mathbf{F}_A - \mathbf{M}_c - \mathbf{S}^B_{r_{BM}}\mathbf{T}^T_{BP}\mathbf{S}^P_{\omega_B}\mathbf{I}_{AM}\bar{\mathbf{V}} - \mathbf{T}^T_{BP}\mathbf{S}^P_{\omega_B}\mathbf{I}_{AI}\mathbf{T}_{BP}\omega_B - \mathbf{S}^B_{r_{BM}}\mathbf{I}'_{AM}\mathbf{S}^B_{\omega_B}\mathbf{T}_{IB}\mathbf{V}_{A/I} - \mathbf{S}^B_{\omega_B}\mathbf{I}_B\omega_B \tag{23}$$

Table 1 Parafoil and payload physical parameters

Parameter	Value	Units	Parameter	Value	Units
C_{D0}	0.15	-	C_{nr}	−0.02	-
$C_{D\alpha^2}$	0.90	-	$C_{n\delta a}$	0.004	-
$C_{Y\beta}$	−0.15	-	C_{DS}	0.40	-
C_{L0}	0.25	-	A	0.012	kg
$C_{L\alpha}$	0.68	-	B	0.032	kg
C_{lp}	−0.355	-	C	0.423	kg
$C_{l\delta a}$	−0.00032	-	P	0.054	kg · m²
C_{m0}	0.0	-	Q	0.014	kg · m²
C_{mq}	−0.265	-	R	0.0024	kg · m²

The 9-DOF equations of motion for the parafoil/payload body can be determined by solving the preceding dynamic equations in combination with the kinematic equations in Eqs. (6), (7), and (10).

V. Model Comparison

Flight-test initial conditions and the miniature parafoil system discussed in Sections II and III were employed in the simulation. The simulation is started at zero cross range and down range, from 400 m above sea level, with payload and parafoil pitch angles of −1.7 deg and −0.3 deg, respectively. The velocity components are u_c being 6.7 m/s, w_c being 4.2 m/s, and all other states zero. Aerodynamic coefficients are estimated from flight test data using standard methods, as described in Jategaonkar [20] whereas the apparent mass coefficients for the canopy are estimated using Lissaman and Brown [3]; both are provided in Table 1.

Inertia matrices for both the parafoil and payload are provided here, with both having units of kg · m²:

$$\mathbf{I}_B = \begin{bmatrix} 0.042 & 0 & -0.007 \\ 0 & 0.027 & 0 \\ -0.007 & 0 & 0.054 \end{bmatrix} \tag{24}$$

$$\mathbf{I}_S = \begin{bmatrix} 0.013 & 0 & 0 \\ 0 & 0.0081 & 0 \\ 0 & 0 & 0.0069 \end{bmatrix} \tag{25}$$

Vectors from the point C to the payload mass center, parafoil mass center, and canopy rotation point are $\mathbf{r}_{CS} = 0.09\mathbf{k}_S$ m, $\mathbf{r}_{CB} = 0.15\mathbf{i}_B - 0.69\mathbf{k}_B$ m, and $\mathbf{r}_{CR} = -0.15\mathbf{i}_B - 0.82\mathbf{k}_B$ m, respectively. Vectors from the canopy rotation point to the parafoil aerodynamic center and apparent mass center are $\mathbf{r}_{RP} = 0.19\mathbf{i}_P$ m and $\mathbf{r}_{RM} = 0.18\mathbf{i}_P + 0.061\mathbf{k}_P$ m, respectively. The rotational stiffness and

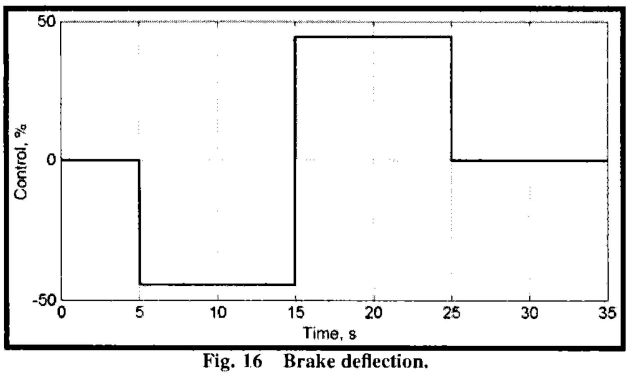

Fig. 16 Brake deflection.

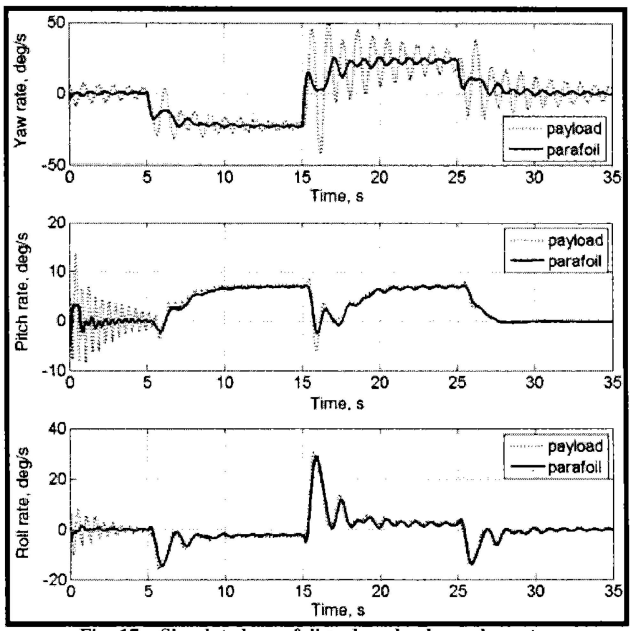

Fig. 17 Simulated parafoil and payload angular rates.

damping from risers are assumed to be constant and estimated to be −0.27 N-m/rad and 0.0 N-m-s/rad from flight-test data.

The 9-DOF model is numerically integrated using a fourth-order Runge-Kutta algorithm with time steps of 0.01 s. Simulations were completed under a situation similar to that experienced by the system in the flight test with a series of 44% left and right brake deflections, as shown in Fig. 16. Initial roll, pitch, and yaw rates for the parafoil and payload were 0.1 rad/s and −0.1 rad/s, respectively, to excite initial motion.

Simulated angular velocities of both the parafoil and payload are shown in Fig. 17. The simulation captures the steady-state yaw rate for both the payload and canopy. The simulated model also accurately replicates the lightly damped payload twist mode, 1.03 Hz in simulation compared with 1.05 Hz from experiments, with an initial yaw rate of approximately 30 deg/s excited while turning. In addition, the parafoil yaw rate oscillates at a significantly lower magnitude than the payload yaw rate, similar to experimental results. The payload twist mode in Fig. 17 is damped despite the rotational damping coefficient K_r in Eq. (13) being zero. Coupling between payload and canopy twisting is the major source of rotation damping. As the payload twists, the canopy responds, and it is the canopy's yaw damping that contributes to the payload twist mode damping. The initial rate disturbance excites the payload and parafoil 2.3 Hz pitch rate modes, and the payload 2.1 Hz roll rate modes with all three decaying within the first 7 s. The remaining simulated pitch rate is dominated by the constant pitch rate achieved by a banked turning vehicle as explained by the three-dimensional kinematics in Eq. (7). Each commanded turn rate, at 5, 15, and 25 s, results in excitation of a roll rate for both bodies. After excitation, the 0.85 Hz canopy roll rate mode can be seen, similar to experimental measurements. The payload also exhibits a similar 0.85 Hz component, but when comparing its magnitude from 20–25 s with the higher frequency mode from 0–5 s, the 0.85 Hz mode is minor. This is consistent with the payload angular velocity amplitude spectrum in Fig. 6.

Payload and canopy yaw are shown below in Fig. 18. Although the total yaw angle of both bodies appears to be similar, the lightly damped 1.05 Hz payload-twisting mode is clearly evident in the relative payload twist with respect to the parafoil body. Simulated pitch and roll of both the payload and canopy exhibit very little dynamic motion. However, steady-state values are in agreement with experimental results, with the pitch angles remaining close to −4 and −16 deg for the payload and parafoil, respectively, and the canopy rolling 18 deg as the system turns. Note that the parafoil pitch in Fig. 19 includes the incidence angle for comparison with experimental data.

When comparing the simulated results with experimental data, an observed difference is the appearance of persistent oscillation in the experimental data, whereas the simulations reach equilibrium. A reason for this is the pristine atmosphere used in the simulation.

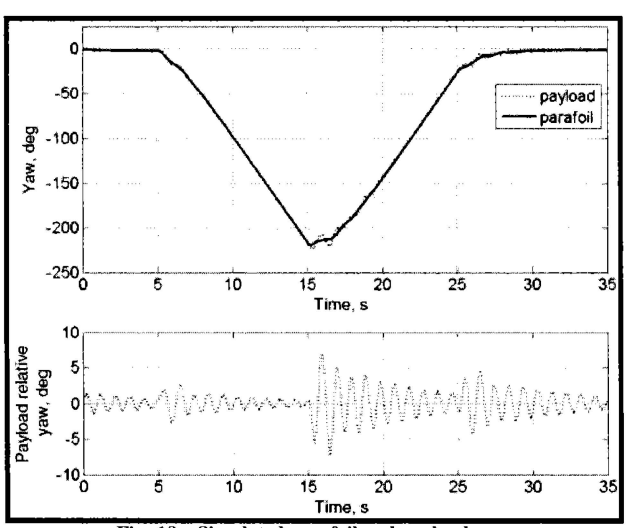

Fig. 18 Simulated parafoil and payload yaw.

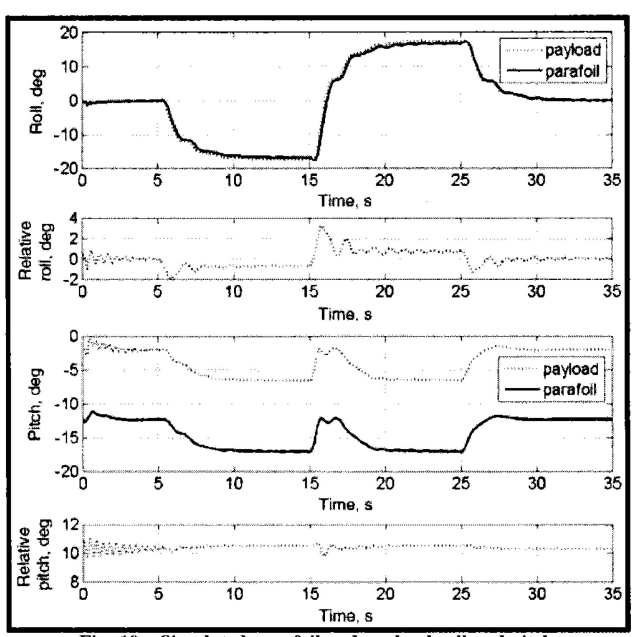

Fig. 19 Simulated parafoil and payload roll and pitch.

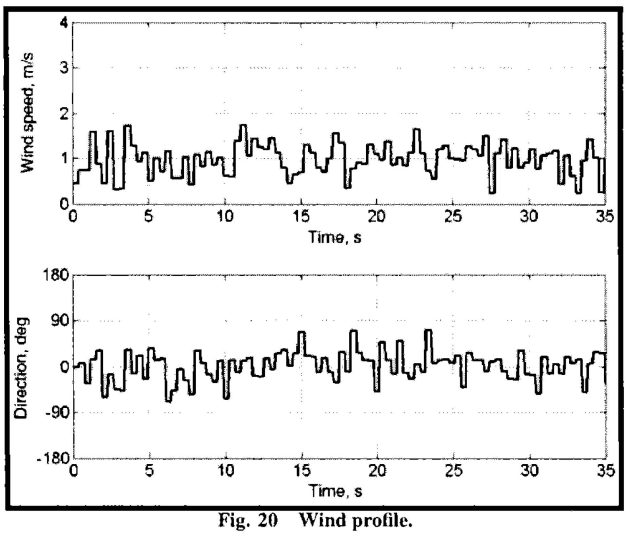

Fig. 20 Wind profile.

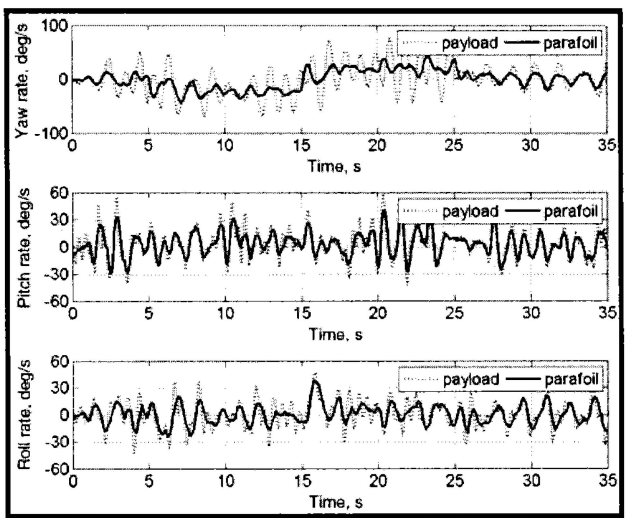

Fig. 21 Parafoil and payload angular rates with simulated winds.

During experiments, the atmosphere experiences changes in wind magnitude, wind direction, updrafts, and turbulence, all continually exciting motion by providing disturbances. To better compare the model with experimental canopy and payload measurements, a

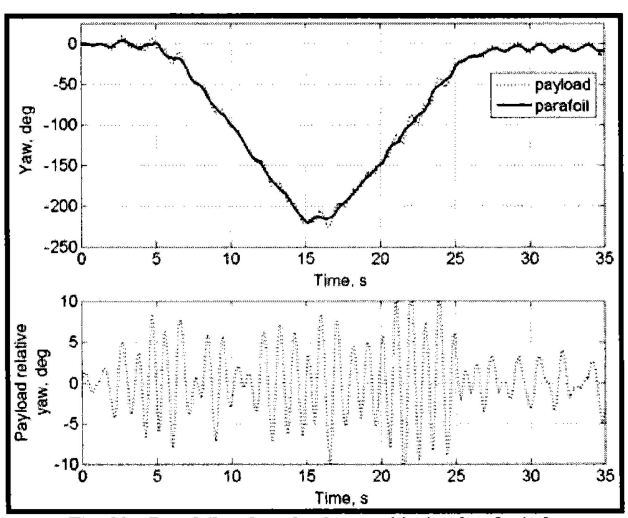

Fig. 22 Parafoil and payload yaw with simulated winds.

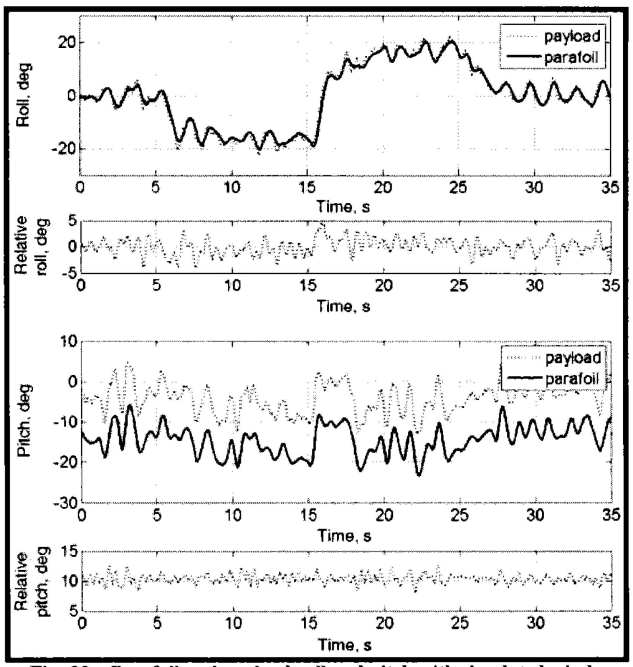

Fig. 23 Parafoil and payload roll and pitch with simulated winds.

variable wind was added. A variable wind was created using a 1 m/s mean wind and normally distributed horizontal variations with a standard deviation of 0.6 m/s at 2.5 Hz. The horizontal wind speed and direction are shown in Fig. 20. The final wind profile has small magnitudes when compared with the system speed and does not significantly alter the gross motion. In essence, it only provides input disturbances to the model.

Figures 21–23 show the preceding simulation with the addition of a variable wind. The main oscillatory modes are still identifiable, but motion is now continually excited, as in the experimental system. Relative twisting between the payload and canopy in Fig. 22 now maintains a magnitude of 8 deg throughout the simulation. Similarly, the payload and canopy have a small 5 deg persistent rolling superposed on the larger rolling motion during turns. Disturbances from the added wind now mask the small pitch variations from turning seen in Fig. 19, which is also consistent with observed measurements. In general, just as it was on the experimental system, the parafoil canopy amplitude of motion was less than the payload. Comparing pitch rates in Figs. 12 and 21 shows that, even with variable winds exciting general persistent motion, the 2.1–2.3 Hz component in simulation is not as predominant as in the experimental measurements. The model captures the 2.3 Hz pitch rate mode, as seen in Fig. 17, when excited by initial pitch rates, rather than disturbance forces. Excitation of this mode during experiments may be originating from either the canopy breathing from flexibility or pitching due to translation of the payload with respect to the parafoil as identified in Strickert [15]. Both effects are not considered in the 9-DOF model.

VI. Conclusions

Miniature wireless inertial sensors were developed, successfully integrated into a parafoil canopy, and used to measure the relative canopy-payload motion in flight. Experimental measurements of a miniature parafoil-payload system were completed using a payload riser configuration that achieved a high level of restriction to relative motion. Despite the designed restriction on relative motion, amplitude spectrums of the canopy and payload differed substantially. The payload had larger amplitude motion, which was of higher frequency than the canopy. The relative motion with largest amplitude was the payload-twisting mode. The lightly damped mode originated from twisting in the suspension lines that allows the payload to twist relative to the canopy. Large amplitude twisting was observed just

after canopy opening with smaller twisting motion excited when turning. The motion was essentially limited to the payload, with only a small amount of canopy twisting measured in response.

Based on inspection of the experimental riser connection, modelers could reasonably justify a number of model orders ranging from a rigid 6-DOF to any of the various multibody models that include relative twisting, pitching, and rolling. These experimental results suggest that a 6-DOF model may be inadequate to capture significant motion of the system. A 9-DOF model was used to show that all significant relative parafoil canopy-payload motion could be captured even though the actual payload connection was approximated by a theoretical gimbaled confluence. The model was able to predict both the payload-twisting mode, using a simple linear line twist model, and the smaller canopy-payload pitching and rolling motion.

References

[1] Benney, R., McGrath, J., McHugh, J., Meloni, A., Noetscher, G., Tavan, S., and Patel, S., "DOD JPADS Programs Overview & NATO Activities," *19th AIAA Aerodynamic Decelerator Systems Technology Conference and Seminar*, AIAA Paper 2007-2576, Williamsburg, VA, May 2007.

[2] Benney, R., Henry, M., Lafond, K., Meloni, A., and Patel, S., "DOD New JPADS Programs & NATO Activities," *Proceedings of the 20th AIAA Aerodynamic Decelerator Systems Technology Conference and Seminar*, AIAA Paper 2009-2952, Seattle, WA, May 2009.

[3] Lissaman, P., and Brown, G., "Apparent Mass Effects on Parafoil Dynamics," *12th AIAA Aerodynamic Decelerator Systems Technology Conference and Seminar*, AIAA Paper 1993-1236, London, England, U.K., May 1993, pp. 233–239.

[4] Jann, T., "Aerodynamic Model Identification and GNC Design for the Parafoil-Load System ALEX," *AIAA 16th Aerodynamic Decelerator Systems Technology Conference and Seminar*, AIAA Paper 2001-2015, Boston, MA, May 2001, pp. 155–165.

[5] Barrows, T., "Apparent Mass of Parafoils with Spanwise Camber," *Journal of Aircraft*, Vol. 39, No. 3, 2002, pp. 445–451. doi:10.2514/2.2949

[6] Slegers, N., and Costello, M., "Model Predictive Control of a Parafoil and Payload System," *Journal of Guidance, Control, and Dynamics*, Vol. 28, No. 4, 2005, pp. 816–821. doi:10.2514/1.12251

[7] Slegers, N., Beyer, E., and Costello, M., "Use of Variable Incidence Angle for Glide Slope Control of Autonomous Parafoil," *Journal of Guidance, Control, and Dynamics*, Vol. 31, No. 3, 2008, pp. 585–596. doi:10.2514/1.32099

[8] Mortaloni, P., Yakimenko, O., Dobrokhodov, V., and Howard, R., "On the Development of a Six-Degree-of-Freedom Model of a Low-Aspect-Ratio Parafoil Delivery System," *17th AIAA Aerodynamic Decelerator Systems Technology Conference and Seminar*, AIAA Paper 2003-2105, Monterey, CA, May 2003, pp. 40–49.

[9] Slegers, N., and Costello, M., "Aspects of Control for a Parafoil and Payload System," *Journal of Guidance, Control, and Dynamics*, Vol. 26, No. 6, 2003, pp. 898–905. doi:10.2514/2.6933

[10] Mooij, E., Wijnands, Q., and Schat, B., "9-DOF Parafoil/Payload Simulator Development and Validation," *AIAA Modeling and Simulation Technologies Conference and Exhibit*, AIAA Paper 2003-5459, Austin, TX, Aug 2003.

[11] Müller, S., Wagner, O., and Sachs, G., "A High-Fidelity Nonlinear Multibody Simulation Model for Parafoil Systems," *17th AIAA Aerodynamic Decelerator Systems Technology Conference and Seminar*, AIAA Paper 2003-2120, Monterey, CA, May 2003, pp. 149–158.

[12] Redelinghuys, R., "A Flight Simulation Algorithm for a Parafoil Suspending an Air Vehicle," *Journal of Guidance, Control, and Dynamics*, Vol. 30, No. 3, 2007, pp. 791–803. doi:10.2514/1.25074

[13] Slegers, N., "Effects of Canopy-Payload Relative Motion on Control of Autonomous Parafoils," *Journal of Guidance, Control, and Dynamics*, Vol. 33, No. 1, 2010, pp. 116–125. doi:10.2514/1.44564

[14] Strickert, G., and Witte, L., "Analysis of the Relative Motion in a Parafoil-Load-System," *16th AIAA Aerodynamic Decelerator Systems Technology Conference*, AIAA Paper 2001-12013, Boston, MA, May 2001.

[15] Strickert, G., "Study on the Relative Motion of Parafoil-Load-Systems," *Aerospace Science and Technology*, Vol. 8, No. 6, 2004, pp. 479–488. doi:10.1016/j.ast.2004.04.003

[16] Strickert, G., and Jann, T., "Determination of the Relative Motion Between Parafoil Canopy and Load Using Advanced Video-Image Processing Techniques," *15th AIAA Aerodynamic Decelerator Systems Technology Conference*, AIAA Paper 1999-1754, Toulouse, France, May 1999, pp. 410–417.

[17] Slegers, N., and Yakimenko, O., "Terminal Guidance of Autonomous Parafoils in High Wind-to-Airspeed Ratios," *Proceedings of the Institution of Mechanical Engineers, Part G: Journal of Aerospace Engineering*, Vol. 225, No. 3, 2011, pp. 336–346.

[18] Yakimenko, O., Slegers, N., and Tiaden, R., "Development and Testing of the Miniature Aerial Delivery System," *20th AIAA Aerodynamic Decelerator Systems Technology Conference*, AIAA Paper 2009-2980, Seattle, WA, 2009.

[19] Blevins, R., *Formulas for Natural Frequency and Mode Shape*, Van Nostrand Reinhold Co., New York, 1979.

[20] Jategaonkar, R. V., *Flight Vehicle System Identification: A Time Domain Approach*, AIAA Education Series, Reston, VA, 2006.